NIH Public Access

Author Manuscript

Sci Transl Med. Author manuscript; available in PMC 2015 October 22.

Published in final edited form as:

Sci Transl Med. 2014 October 22; 6(259): 259ra146. doi:10.1126/scitranslmed.3009815.

Imaging Enterobacteriaceae infection in vivo with ^{18}F-fluorodeoxysorbitol positron emission tomography

Edward A. Weinstein[1,2,*], **Alvaro A. Ordonez**[1,3,*], **Vincent P. DeMarco**[3], **Allison M. Murawski**[3], **Supriya Pokkali**[3], **Elizabeth M. MacDonald**[1,3], **Mariah Klunk**[1,3], **Ronnie C. Mease**[4], **Martin G. Pomper**[1,4], and **Sanjay K. Jain**[1,3,†]

[1]Center for Infection and Inflammation Imaging Research, Johns Hopkins University School of Medicine, Baltimore, MD 21287, USA

[2]Department of Medicine, Johns Hopkins University School of Medicine, Baltimore, MD 21287, USA

[3]Department of Pediatrics, Johns Hopkins University School of Medicine, Baltimore, MD 21287, USA

[4]Russell H. Morgan Department of Radiology and Radiological Science, Johns Hopkins University School of Medicine, Baltimore, MD 21287, USA

Abstract

The Enterobacteriaceae are a family of rod-shaped Gram-negative bacteria that normally inhabit the gastrointestinal tract and are the most common cause of Gram-negative bacterial infections in humans. In addition to causing serious multidrug-resistant, hospital-acquired infections, a number of Enterobacteriaceae species are also recognized as biothreat pathogens. As a consequence, new tools are urgently needed to specifically identify and localize infections due to Enterobacteriaceae and to monitor antimicrobial efficacy. In this report, we used commercially available 2-[^{18}F]-fluorodeoxyglucose (^{18}F-FDG) to produce 2-[^{18}F]-fluorodeoxysorbitol (^{18}F-FDS), a radioactive probe for Enterobacteriaceae, in 30 min. ^{18}F-FDS selectively accumulated in Enterobacteriaceae, but not in Gram-positive bacteria or healthy mammalian or cancer cells in vitro. In a murine myositis model, ^{18}F-FDS positron emission tomography (PET) rapidly differentiated true infection from sterile inflammation with a limit of detection of 6.2 ± 0.2 $\log_{10}$ colony-forming units (CFU) for *Escherichia coli*. Our findings were extended to models of mixed Gram-positive and Gram-negative thigh co-infections, brain infection, *Klebsiella* pneumonia, and mice

---

[†] Corresponding author. sjain5@jhmi.edu.

[*] These authors contributed equally to this work.

Competing interests: E.A.W., A.A.O., M.K., M.G.P., and S.K.J. are inventors for an International patent PCT/US13/059897, “Bacteria-specific labeled substrates as imaging biomarkers to diagnose, locate and monitor infections” filed by Johns Hopkins University.

SUPPLEMENTARY MATERIALS

www.sciencetranslationalmedicine.org/cgi/content/full/6/259/259ra146/DC1

Author contributions: E.A.W., A.A.O., and S.K.J. designed the research. E.A.W. and R.C.M. designed the protocols for synthesizing ^{18}F-FDS. E.A.W., A.M.M., and E.M.M. synthesized ^{18}F-FDS for the experiments. E.A.W., A.A.O., A.M.M., and E.M.M. performed the in vitro assays. A.A.O., V.P.D., and M.K. developed the animal models and performed imaging. A.A.O., V.P.D., and A.M.M. performed biodistribution studies. A.A.O. and S.P. performed microbiological and histological studies. S.P. performed protein estimations. A.A.O. performed the statistical analyses. E.A.W., A.A.O., M.G.P., and S.K.J. analyzed the data. All authors wrote the paper. S.K.J. provided funding and supervised the project.

NIH-PA Author Manuscript

NIH-PA Author Manuscript

NIH-PA Author Manuscript

NIH-PA Author Manuscript NIH-PA Author Manuscript NIH-PA Author Manuscript

undergoing immunosuppressive chemotherapy. This technique rapidly and specifically localized infections due to Enterobacteriaceae, providing a three-dimensional holistic view within the animal. Last, ^{18}F-FDS PET monitored the efficacy of antimicrobial treatment, demonstrating a PET signal proportionate to the bacterial burden. Therapeutic failures associated with multidrug-resistant, extended-spectrum β-lactamase (ESBL)–producing *E. coli* infections were detected in real time. Together, these data show that ^{18}F-FDS is a candidate imaging probe for translation to human clinical cases of known or suspected infections owing to Enterobacteriaceae.

INTRODUCTION

The Enterobacteriaceae are the most common cause of Gram-negative bacterial infections in humans and include prominent pathogens such as *Yersinia* spp., *Escherichia coli*, *Klebsiella* spp., and *Enterobacter* spp. Several Enterobacteriaceae species are recognized as biothreat pathogens by the U.S. Centers for Disease Control and Prevention (CDC), and also are a cause of serious multidrug-resistant (MDR) hospital-acquired infections (1). For example, *E. coli*, a prominent pathogen within this family, is the most commonly isolated bacteria in clinical laboratories (2) and is a notorious source of life-threatening MDR infections in cancer patients.

When an infection is suspected, but occurs at an unknown location or deep within the body, noninvasive anatomic imaging techniques are used to identify a site of interest for biopsy and microbial culture. The most common approaches are computed tomography (CT), magnetic resonance imaging (MRI), and nuclear medicine techniques such as ^{111}In-oxine–labeled white blood cell imaging and 2-[^{18}F]-fluorodeoxyglucose (^{18}F-FDG) positron emission tomography (PET). Each modality provides limited clinical information. CT and MRI both reveal structural abnormalities that are nonspecific and often occur late in a disease process. Labeled leukocytes, generated through a multistep process, produce nonspecific signals and may have limited penetration into diseased tissues (3). ^{18}F-FDG PET has emerged as a highly sensitive imaging method, but lacks specificity and cannot differentiate among oncologic, inflammatory, or infectious processes. Moreover, these imaging techniques are dependent on host inflammatory responses to infection, which may be reduced or absent in immunosuppressed patients (for example, cancer chemotherapy, HIV/AIDS, or organ transplant) who are most at risk for infection. Follow-up microbiological or molecular testing is still required after performing any of these imaging techniques to establish a diagnosis, resulting in a prolonged, uncertain process that takes several days. Last, current technologies fail to provide rapid feedback about the effect, or adequacy, of a selected antimicrobial regimen. Therefore, there is a need for rapid, whole-patient imaging techniques that could localize a pathogen with specificity and provide a quantitative readout of disease burden in response to treatment.

In clinical microbiology, pathogenic Enterobacteriaceae are differentiated from other organisms by selective metabolism. Sorbitol is a metabolic substrate for Enterobacteriaceae, but is more commonly known as a “sugar-free” sweetener. We hypothesized that a positron-emitting analog of sorbitol, 2-[^{18}F]-fluorodeoxysorbitol (^{18}F-FDS), first described for tumor imaging (4), would be a suitable probe to selectively label and tomographically image these

NIH-PA Author Manuscript

NIH-PA Author Manuscript

NIH-PA Author Manuscript

bacteria in vivo. Using the methods described in (4), we derived ^{18}F-FDS from commercial ^{18}F-FDG to confer selectivity for Enterobacteriaceae for use as a diagnostic tool with broad utility. We describe our development of the radioprobe in several preclinical models of infection by Enterobacteriaceae and demonstrate that serial imaging over time can provide predictive information on the success of a chosen antimicrobial treatment regimen. The pathogen-specific mechanism of ^{18}F-FDS imaging could be used to identify and monitor known or suspected infections caused by Enterobacteriaceae.

RESULTS

^{18}F-FDS is taken up rapidly and specifically by a range of Enterobacteriaceae

Cultures of *E. coli* and *Klebsiella pneumoniae* were selected to assess ^{18}F-FDS accumulation in vitro. These two Gram-negative enteric species readily incorporated ^{18}F-FDS (Fig. 1A). *Staphylococcus aureus*, a Gram-positive bacterium, did not accumulate ^{18}F-FDS but did accumulate ^{18}F-FDG. Heat-killed bacteria did not incorporate either probe. *E. coli* cultures were also co-incubated with ^{18}F-FDS and increasing concentrations of unlabeled sorbitol (Fig. 1B). ^{18}F-FDS uptake was outcompeted by concentrations of sorbitol above 40 μg/ml, suggesting that uptake does reach a point of saturation, presumably in a transporter-driven process.

The presence of the sorbitol-6-phosphate dehydrogenase (*srlD*) gene cassette responsible for sorbitol metabolism has been noted within the annotated genome of *E. coli* (5, 6). To predict the range of bacteria capable of ^{18}F-FDS uptake and likely detection by PET, the *srlD* gene was used to query the UniProtKB database of genome-sequenced bacterial species (Fig. 1C). Representative bacteria from that panel were tested to assess ^{18}F-FDS uptake. Members of the Enterobacteriaceae family accumulated ^{18}F-FDS, whereas Gram-positive bacteria, such as *Enterococcus*, *Staphylococcus*, and *Streptococcus* spp., and the aerobic Gram-negative rod *Pseudomonas aeruginosa* did not accumulate the probe (Fig. 1D). Additionally, mammalian cells and tumor cell lines did not accumulate ^{18}F-FDS, with an uptake almost 1000-fold higher in *E. coli* than in mammalian cells (Fig. 1E). Together, these data demonstrate the selectivity of ^{18}F-FDS.

^{18}F-FDS PET can rapidly differentiate infection sites from sterile inflammation

We next investigated whether ^{18}F-FDS PET could distinguish *E. coli* infection from sterile inflammation in vivo. Mice were inoculated with live *E. coli* into the right thigh and a 10-fold higher burden of heat-killed *E. coli* into the left thigh (sterile inflammation). ^{18}F-FDS readily concentrated in the infected right thigh, but not in the sterile, inflamed left thigh (Fig. 2A). Reference imaging with ^{18}F-FDG could not qualitatively distinguish the infected right thigh from the sterile, inflamed left thigh (Fig. 2A).

Next, to quantify PET signal intensity, we drew spherical regions of interest (ROIs) within the thighs on the basis of anatomical localization from CT. ^{18}F-FDS produced 7.3-fold higher signal intensity in the infected right thigh compared to the sterile, inflamed left thigh (Fig. 2B). In contrast, ^{18}F-FDG did not produce significantly different signal intensities between the thighs (Fig. 2C). We then surgically resected tissue from the mice postmortem

NIH-PA Author Manuscript

NIH-PA Author Manuscript

NIH-PA Author Manuscript

to confirm the PET findings with a γ counter. In agreement with the PET signal, there was 7.9-fold higher γ emission from the infected right thigh than the sterile, inflamed left thigh (Fig. 2B). Similar to in vivo data, ^{18}F-FDG did not discriminate the infection from the sterile inflammation in the thighs (Fig. 2C). It should also be noted that ^{18}F-FDG counts from both the *E. coli*–infected (1.7-fold) and sterile, inflamed control thighs (1.7-fold) were significantly higher than the uninflamed, uninfected deltoid muscle (Fig. 2C). However, no differences in ^{18}F-FDS counts were noted between the sterile, inflamed control thighs and the uninflamed deltoid, further confirming that ^{18}F-FDS was specific for infection and not taken up at sites of sterile inflammation. Postmortem tissue histology of the thighs verified the presence inflammatory cells and Gram-negative bacteria in the *E. coli*–infected right thigh (Fig. 2D) and inflammatory cells without bacteria, in the uninfected (but inflamed) left thigh (Fig. 2E). More extensive tissue histology is given in fig. S1. A three-dimensional ^{18}F-FDS PET/CT image of the *E. coli*–infected mouse is shown in movie S1.

We then extended our findings to a mouse model of infection during immunosuppression. In this model, mice were infected with *E. coli* during the course of cancer chemotherapy. The same experiments as in Fig. 2 were performed while treating mice with a neutropenia-inducing cyclophosphamide regimen (days 1 and 4), as described in (7). The absence of a normal immune response did not impede detection of infection in the right thigh, but not the inflamed left thigh, by ^{18}F-FDS (fig. S2). ^{18}F-FDG was not examined in comparison for this study.

^{18}F-FDS was also evaluated in brain infection and tumor models to confirm specificity for infection versus oncologic processes. ^{18}F-FDS PET intensities in *E. coli*–infected brains, human glioblastoma xenografts (U87MG), and normal brains were compared. The data demonstrated a significantly higher uptake in the *E. coli*–infected brain versus brain tumor or normal brain (Fig. 3A). ^{18}F-FDS PET could localize the *E. coli* brain infection, but no signal was seen for the normal brain or glioblastoma (Fig. 3B). ^{18}F-FDS was also evaluated in a dual brain tumor and *E. coli* thigh infection in the same animal, which demonstrated a significantly higher PET signal intensity in *E. coli*–infected thighs compared to U87MG brain tumors (Fig. 3C). Finally, dynamic ^{18}F-FDS PET imaging (over 120 min) in mice with U87MG brain tumors was performed (fig. S3). Although there was some initial uptake by the tumor tissues, the PET signal dissipated after 60 min. By comparison, signals from infection could be seen consistently even at 120 min (Fig. 3B).

^{18}F-FDS is selective for Enterobacteriaceae in mixed infections

Immunosuppressed mice were inoculated with live *E. coli* and *S. aureus* in the right and left thighs, respectively. Consistent with in vitro uptake data, ^{18}F-FDS readily concentrated in the *E. coli*–infected right thigh, but not in the *S. aureus*–infected left thigh (Fig. 4A). ^{18}F-FDG PET could not distinguish the *E. coli* infection from the *S. aureus* infection (Fig. 4A). The ^{18}F-FDS PET signal intensity and tissue biodistribution were both higher at the site of the *E. coli* infection (right thigh) compared with those at the site of the *S. aureus* infection (left thigh) (Fig. 4B). There was no significant difference between thighs for^{18}F-FDG (Fig. 4C). Postmortem tissue histology of the thighs verified the presence of bacteria in the lesions (Fig. 4D). At the time of imaging, there were 30-fold higher numbers of *S. aureus* [8.3 ± 0.3

NIH-PA Author Manuscript

NIH-PA Author Manuscript

NIH-PA Author Manuscript

$\log_{10}$ colony-forming units (CFU)] than *E. coli* (6.8 ± 0.7 $\log_{10}$ CFU) in the respective thighs. Moreover, we could reliably detect as few as 6.2 ± 0.2 $\log_{10}$ CFU of *E. coli* (at the time of imaging) with ^{18}F-FDS PET in one cohort of the dually infected myositis mice (Fig. 4E).

Enterobacteriaceae, and in particular *K. pneumoniae*, are an important cause of MDR hospital-acquired pneumonias, which cannot be easily distinguished from other bacteria (8–10). In a pulmonary infection model, ^{18}F-FDS readily localized to the areas of lung infiltration observed by CT (Fig. 5A). PET signal intensity and corresponding postmortem tissue bio-distribution were significantly higher at the site of the *K. pneumoniae* pulmonary infection than in the uninfected control lungs (Fig. 5, B and C).

^{18}F-FDS can monitor antimicrobial efficacy in MDR infections

Enterobacteriaceae are becoming increasingly resistant to many classes of antimicrobials, and consequent treatment failuresare of great concern to public health (11–14). For example, mortality can approach as high as 60% in infections associated with drug-resistant extended-spectrum β-lactamase (ESBL)–producing Enterobacteriaceae (14). ^{18}F-FDS was evaluated against 15 random ESBL-producing clinical strains, which demonstrated substantial uptake in all isolates (Fig. 6A). For comparison to Gram-positive cellular uptake (at 0 Bq per 10^6 cells), see Fig. 1D.

Immunosuppressed mice were inoculated with drug-susceptible or drug-resistant (ESBL-producing) *E. coli* into the right thigh and a 10-fold higher burden of the corresponding heat-killed *E. coli* strain into the left thigh. ^{18}F-FDS PET imaging was performed before and after the administration of ceftriaxone, a commonly used antimicrobial that is effective against drug-susceptible *E. coli* but ineffective against ESBL producers. Corresponding to the bacterial CFU, ^{18}F-FDS PET signal disappeared with treatment in mice infected with drug-susceptible *E. coli*, but persisted in mice infected with the drug-resistant *E. coli* (Fig. 6B). An increase in CFU measured immediately after the completion of imaging corresponded with disease progression. The inadequately treated mice clinically appeared sick, manifesting ruffled fur, hunched posture, inactivity, and increased respiratory rate, all consistent with sepsis, and were euthanized per protocol. Rapid assessment of a therapeutic failure would be highly valuable for the management of seriously ill patients.

DISCUSSION

The Enterobacteriaceae produce a range of human disease, from lethal fulminant pneumonias to deep-seated MDR infections. When serious infections are suspected, patients are often treated empirically with a combination of broad-spectrum antimicrobials while awaiting culture results that provide information on the bacterial class and species causing the infection, as well as drug susceptibilities. These traditional diagnostic techniques can take several days and may not provide reliable information, because blood cultures could have high contamination rates, prompting several groups to propose validation rules (15, 16). The combination of time and effort required for proper antimicrobial selection has become a barrier leading to uncertainty and indiscriminate broad-spectrum antimicrobial use (17). Judicious use could reduce the emergence of drug resistance, increase patient safety,

NIH-PA Author Manuscript
NIH-PA Author Manuscript
NIH-PA Author Manuscript

and save billions of dollars for the U.S. health care system alone (18). Consequently, there is a need to diagnose infections quickly, including deep-seated, difficult-to-access lesions due to Enterobacteriaceae.

For oncological applications, ^{18}F-FDG PET can detect on the order of 5 to 6 $\log_{10}$ cells (19), which is near the limit of detection for CT imaging. However, detection of infection by current imaging techniques is variable and dependent on host responses, as well as the site and type of infection. In our study, ^{18}F-FDS PET imaging accurately identified the magnitude and location of infections caused by Enterobacteriaceae in vivo in mice. ^{18}F-FDS produced a strong signal with minimal background noise, allowing for the detection of as few as 6.2 ± 0.2 $\log_{10}$ CFU of *E. coli* as enumerated from the infected tissues after imaging. This is a promising threshold because clinically relevant bacterial infections have high bacterial burdens [8.3 $\log_{10}$ CFU/ml (20)] and can be as large as several centimeters in diameter with volumes of tens to hundreds of milliliters (21, 22). Therefore, the ^{18}F-FDS limit of detection suggests that a positive signal would provide an early indication of infection in the host, although the sensitivity and specificity of this technique in the clinical setting remain to be determined. We predict that our results with *E. coli* and *K. pneumoniae* could be extended to detect other members of the Enterobacteriaceae family, such as *Yersinia* spp. or *Salmonella* spp., which demonstrate substantial ^{18}F-FDS uptake in vitro (Fig. 1D).

We did not use background subtraction in any of our images. In some images, an extraneous signal was noted in the mouse intestine, which corresponded to the biliary excretion of ^{18}F-FDS and subsequent uptake by gut flora. The source of this signal was variably placed depending on peristalsis of the stool pellet in the colon. Anatomic localization with CT would be able to distinguish an intraluminal PET signal from an extraluminal PET signal in abdominal infections. Additionally, there were signals from the kidneys and bladder owing to the urinary clearance of ^{18}F-FDS. Elimination of a probe by hepatic or renal routes would be expected for any radiopharmaceutical, and we believe that this would not be a major limitation to the clinical use of ^{18}F-FDS. By delaying PET image acquisition until a patient urinates (or by use of a urinary catheter), kidney infections could potentially be visualized. For example, prostate tissue has been successfully imaged with renally cleared PET probes using this approach (23).

Li *et al*. (4) were the first to chemically reduce ^{18}F-FDG into ^{18}F-FDS for the molecular imaging of brain tumors. We therefore used the same brain tumor model and demonstrated that the *E. coli* thigh infection produced a significantly higher ^{18}F-FDS PET intensity compared to the signal from the U87MG human brain tumor (Fig. 3). To consider the possibility of differential uptake pharmacokinetics between brain and peripheral tissues, we developed an *E. coli* brain infection model that confirmed higher ^{18}F-FDS uptake in an *E. coli* infection than in a brain tumor. We note that this finding is consistent with our in vitro data indicating a lack of ^{18}F-FDS uptake by eukaryotic cells (Fig. 1E), as well as data presented in the study by Li *et al*. (4). There is no selective transporter for ^{18}F-FDS entry into eukaryotic cells, and the substitution of the hydroxyl group by fluorine at the C-2 position completely abrogates the recognition by mammalian sorbitol dehydrogenase (24). Moreover, comparisons by Li *et al.* were made in the context of low signal with high

NIH-PA Author Manuscript

NIH-PA Author Manuscript

NIH-PA Author Manuscript

background at earlier time points (5 to 60 min). We therefore performed dynamic ^{18}F-FDS PET imaging over 120 min in mice with U87MG brain tumors and demonstrated initial uptake, which dissipated over time (fig. S3). This suggests that the results presented by Li *et al.* may be consistent with a nonspecific blood pool effect, that is, capillary leak at the site of inflammation or tumor. Detection of brain infections, however, is a new finding for ^{18}F-FDS and, to our knowledge, has not been demonstrated for other probes in development.

Although several promising optical imaging probes have been reported to detect bacterial infections (25–28), these probes are not yet clinically translatable. Despite the excellent sensitivity of optical imaging, the approach is limited by the absorption of light within deep tissues and, therefore, applicable to imaging of small animals or superficial sites only. The sensitivity of optical imaging (pico- to femtomolar) is significantly higher than that of PET or single-photon emission computed tomography (SPECT) (nano- to picomolar) (29). Therefore, human translation (optical to PET or SPECT) will lower sensitivity by several orders of magnitude. Moreover, for conversion to PET or SPECT, an optical probe will need to be labeled with a high-energy emitting isotope, which may change its chemical properties or target binding characteristics. PET or SPECT imaging intrinsically takes advantage of high-energy photons that can radiate out from the deepest structures within the body.

Several radiolabeled antibiotics and peptides, such as ^{99m}Tc-ciprofloxacin, have been evaluated in clinical studies for diagnosing infections (30, 31). However, bacteria-specific antibiotics and peptides are designed to kill or disable bacteria at the lowest possible concentration; therefore, they may not be ideal for imaging purposes owing to the lack of signal amplification from probe accumulation by the bacteria. Although safe, ^{99m}Tc-ciprofloxacin demonstrated variable specificity in clinical studies and an inability to reliably differentiate infection from sterile inflammatory processes (32–35). Radiolabeled peptides similarly demonstrated varying degrees of specificity in their ability to detect infection (36). *S. aureus* endocarditis has been detected in mice with labeled prothrombin, which binds to the staphylococcal coagulase (37). However, this probe is not specific for *S. aureus*, because it is a prothrombin analog, which has the potential for activation and false-positive signaling by noninfectious processes or by other types of bacteria. ^{124}I-FIAU is an example of a PET probe for bacterial infections (38) but is at least one to two orders of magnitude less sensitive than ^{18}F-FDS. Moreover, the synthesis of ^{124}I-FIAU is challenging because it uses I-124 iodide, which could limit its widespread use.

Because antimicrobial selection is dependent on the bacterial class and species causing the infection (for example, vancomycin is used to treat infections with Gram-positive bacteria but has no activity against Gram-negative organisms), a general infection imaging probe, although valuable, may not provide the necessary information to streamline antimicrobial selection. However, imaging probes that are selective for important and common classes of bacterial pathogens could not only diagnose infections noninvasively but also rapidly identify the causative bacterial class and help in the selection of appropriate antimicrobial treatment.

PET is becoming a routine clinical tool, particularly for oncology and neurology, and an increasingly useful array of radioprobes, particularly those radiolabeled with ^{18}F, are

NIH-PA Author Manuscript

NIH-PA Author Manuscript

NIH-PA Author Manuscript

proliferating in the United States and abroad. The pharmacokinetics of ^{18}F-FDS in humans have yet to be established, but the rapid clearance of low molecular weight, short half-life probes, such as ^{18}F-FDS, makes them favorable compared to radio-labeled antibodies, which sometimes require a week to circulate and clear from nontarget sites. Typically, a PET scan is obtained 1 to 2 hours after injection of the radioprobe and can take 15 to 60 min depending on the scan area. ^{18}F-FDS PET could be applied clinically to patients with suspected deep-seated infections due to Enterobacteriaceae, such as intra-abdominal or implant infections or ventilator-acquired pneumonias, and in monitoring infections with drug-resistant Enterobacteriaceae.

Immunosuppressed patients would benefit from noninvasive imaging because a surgical biopsy in itself risks introducing infection. Whole-body scans may be used in patients whose source of infection is not known, whereas targeted scans could be used for monitoring known site(s) of infection. Repeat imaging would be useful if clinical signs and symptoms suggest persistent infection despite antibacterial therapy. CT and MRI cannot monitor acute responses (hours to days), because they reveal structural abnormalities and inflammation, which do not subside rapidly. ^{18}F-FDG PET cannot detect the effect of antibiotics on acute infection (39), and paradoxically, signal intensities may increase acutely owing to inflammation upon effective antimicrobial treatments (40, 41). ^{18}F-FDS PET signal intensities, in contrast, correlate with bacterial burden and would support a clinical decision to change the drug regimen, or proceed to surgical intervention.

In summary, we have developed a diagnostic tool for imaging infections due to Enterobacteriaceae, the most common Gram-negative human bacterial pathogens and a frequent cause of serious drug-resistant hospital-acquired infections. ^{18}F-FDS is inexpensive and can be easily synthesized anywhere in the world where ^{18}F-FDG, the most widely used PET probe, is available. Sorbitol, the radiodecay product, is already approved for use in humans by the U.S. Food and Drug Administration. ^{18}F-FDS could therefore be translated to humans and provide a rapid, noninvasive diagnostic tool to identify and localize infections from Enterobacteriaceae, guide antimicrobial selection, and increase patient safety. In our study, ^{18}F-FDS was identified through a systematic discovery program. Future efforts should focus on discovering class-specific bacterial imaging probes that would detect and differentiate a wide range of pathogenic bacteria.

MATERIALS AND METHODS

Study design

The objective of this study was to test ^{18}F-FDS as a noninvasive imaging probe and diagnostic tool that identifies and localizes infections due to Enterobacteriaceae in vivo. All protocols were approved by the Johns Hopkins Biosafety, Radiation Safety, and Animal Care and Use Committees. Measurement of radioactivity using PET/CT imaging and postmortem biodistribution studies allowed for the quantification of ^{18}F-FDS uptake by Enterobacteriaceae. CFU confirmed the presence of bacteria within the specified organ. Mice were purchased from the same breeding source, housed similarly before infection, and randomly assigned to infected and control groups for experiments. PET/CT images were

NIH-PA Author Manuscript

NIH-PA Author Manuscript

NIH-PA Author Manuscript

acquired using the same parameters. The study was not blinded. All data from the experiments were included in the analyses and are presented in this article.

Synthesis of ^{18}F-FDS

All chemicals used in the study were purchased from commercial vendors and used without purification except where stated. ^{18}F-FDS was generated from commercially available ^{18}F-FDG (PETNET Solutions Inc. or IBA Molecular) using the method described in (4). Briefly, ^{18}F-FDG was reduced with sodium borohydride at 35°C for 30 min before quenching with acetic acid and pH correction to 7.4 with sodium bicarbonate. The product was then passed through an n-alumina Sep-Pak and 0.2-μm filter (Waters Corporation). Chemical purity of the final product, ^{18}F-FDS, was confirmed by high-performance liquid chromatography. Both ^{1}H and ^{13}C nuclear magnetic resonance and mass spectrometry confirmed the structure of the final product.

^{18}F-FDS uptake assays

Bacterial strains purchased from the American Type Culture Collection (ATCC) or 15 drug-resistant (ESBL-producing) *E. coli* strains (random consecutive samples) from the clinical microbiology laboratory (Johns Hopkins Hospital) were aerobically grown to absorbance at 600 nm of 1.0 in Lysogeny Broth (LB). The number of CFU was enumerated by dilution and plated onto solidified LB medium. Probe uptake assays were performed by incubating bacterial cultures with ^{18}F-FDS (20 kBq/ml) at 37°C with rapid agitation. As a control, heat-killed (90°C for 30 min) bacteria were similarly incubated with each probe. Bacteria were pelleted by centrifugation and washed three times with PBS, and the activity for each pellet was measured using an automated γ counter (1282 Compugamma CS Universal gamma counter, LKB Wallac). Six replicates were used for each assay. Counts for each sample were corrected for background and normalized to CFU or total protein. Protein estimation was performed using a Bradford assay (Sigma). For in silico analysis, *E. coli srlD* sequence was queried against the UniProtKB database of genome-sequenced bacterial species. Alignment and percentage identity were then calculated using Clustal Omega (42).

Animal models and infection

CBA/J mice (female, 6 to 8 weeks old) were used for all experiments except those bearing xenografts (athymic nude, male, 10 to 12 weeks). A subset of CBA/J mice were immunosuppressed with cyclophosphamide as described in (7). Mice were injected with different strains of live or heat-inactivated (90°C for 30 min) bacteria. Thigh infections were allowed to develop for 10 and 6 hours in immunocompetent and immunosuppressed mice, respectively. Target implantation for *E. coli* was 7 $\log_{10}$ CFU for all infections, except where indicated. For the dual-infection myositis model, target implantation for *S. aureus* was 7 to 8 $\log_{10}$ CFU, with 10- to 100-fold lower dose used for *E. coli*. The pneumonia model, adapted from (43), was made by intratracheal installation of *K. pneumoniae* (6.5 $\log_{10}$ CFU) into the trachea of sedated, immunosuppressed mice with 5 days of incubation. Brain tumor (5×10^5 U87MG human glioblastoma cells) and infection (7 $\log_{10}$ CFU of *E. coli* in immunosuppressed mice) models were established by inoculations into the right frontal lobe (1.5 mm anterior and 1.34 mm lateral to the bregma, 3.5 mm into the

NIH-PA Author Manuscript NIH-PA Author Manuscript NIH-PA Author Manuscript

parenchyma) through a 50-μm glass capillary needle as described in (44). Brain tumor size at the time of imaging was 30 to 40 mm^3 (based on ex vivo measurements).

PET/CT imaging

Probe (7.4 MBq) was injected via tail vein 120 min (^{18}F-FDS) or 45 min (^{18}F-FDG) before acquiring a 15-min static PET frame using the Mosaic HP (Philips) as described before (40). CT was performed with NanoSPECT/CT (Bioscan). A urinary catheter was placed to empty the bladder during imaging. For quantitative analysis, one to two spherical (3-mm-diameter) ROIs were drawn manually in the thighs of each animal, using CT as a guide. The standardized uptake values (SUVs) were computed using Amide version 1.0.4 (http://www.amide.sourceforge.net), and Amira version 5.4.2 (Visualization Science Group) was used to visualize the images. After imaging, mice were sacrificed to collect tissues for direct γ counting (biodistribution). Some cohorts were also used to determine histology and/or CFU at the time of imaging. The biodistribution data are presented as percent injected dose per gram of tissue (%ID/g). H&E and Gram stains were performed to visualize tissue histology and bacteria, respectively. Tissues were also homogenized in PBS, plated onto solidified LB medium, and incubated overnight at 37°C to enumerate the CFU.

Antimicrobial efficacy studies

E. coli myositis was generated in immunosuppressed mice with drug-susceptible [ceftriaxone minimum inhibitory concentration (MIC), 0.04 μg/ml] or ESBL-producing *E. coli* (ceftriaxone MIC >32 μg/ml). Ceftriaxone (Sigma) was administered subcutaneously at a dose of 5 mg/kg (every 2 hours) for 24 hours (45). Imaging was performed in the same group of animals immediately before starting and after completion of antimicrobial treatment. After the final imaging time point, the same mice were sacrificed to determine CFU. A separate group of similarly infected mice were also sacrificed before the start of antimicrobial treatment to determine the starting CFU. Tissues were homogenized in PBS, plated onto solidified LB medium, and incubated overnight at 37°C to enumerate the CFU. SUV ratios were obtained by normalizing the PET SUV from the infected right thigh with the inflammation control (heat-killed *E. coli* strain) left thigh for each animal.

Statistical analyses

Data from uptake assays are presented as means and SEM and analyzed using unpaired two-tailed Student's *t* test or two-way analysis of variance (ANOVA) with Bonferroni correction (for multiple comparisons) with GraphPad Prism 6.03 (GraphPad Software Inc.). PET SUV and ex vivo tissue biodistribution data are represented as box plots where central bars represent median value, the edges of the boxes represent quartile value, and whiskers show the upper and lower ranges. Statistical comparisons were performed using a two-tailed Mann-Whitney *U* or Kruskal-Wallis (for multiple comparisons) test (GraphPad Software Inc.). Values of $P < 0.05$ were considered statistically significant. Data are presented on a linear scale, except for CFU, which is presented on a logarithmic scale.

Supplementary Material

Refer to Web version on PubMed Central for supplementary material.

NIH-PA Author Manuscript
NIH-PA Author Manuscript
NIH-PA Author Manuscript

Acknowledgments

We thank A. Woods and L. Muller (NIH/National Institute on Drug Abuse) for performance of mass spectrometric analysis; P. Mister and K. Carroll (Johns Hopkins Hospital) for providing the ESBL-producing clinical strains; and O. Wijesekera, H. Guerrero-Cazares, and A. Quinones-Hinojosa (Johns Hopkins Hospital) for the brain infection and tumor models. We also thank C. Sears and W. Bishai (Johns Hopkins Hospital) for comments.

Funding: This study was funded by the NIH Director's New Innovator Award DP2-OD006492 (S.K.J.), as well as R01-HL116316 (S.K.J.), and a subcontract from Harvard University Center for AIDS Research 5P30AI060354-09 (S.K.J.).

REFERENCES AND NOTES

1. Donnenberg, MS. Mandell, Douglas, and Bennett's Principles and Practice of Infectious Diseases. Bennett, JE.; Mandell, GL.; Dolin, R., editors. Vol. chap 218. Elsevier Inc; Philadelphia, PA: 2010. p. 2815-2833.
2. Guentzel, MN. Medical Microbiology. Baron, S., editor. Vol. chap 26. University of Texas Medical Branch at Galveston; Galveston, TX: 1996.
3. Signore A, Glaudemans AW. The molecular imaging approach to image infections and inflammation by nuclear medicine techniques. Ann Nucl Med. 2011; 25:681–700. [PubMed: 21837469]
4. Li ZB, Wu Z, Cao Q, Dick DW, Tseng JR, Gambhir SS, Chen X. The synthesis of ^{18}F-FDS and its potential application in molecular imaging. Mol Imaging Biol. 2008; 10:92–98. [PubMed: 18097725]
5. Lechat P, Hummel L, Rousseau S, Moszer I. GenoList: An integrated environment for comparative analysis of microbial genomes. Nucleic Acids Res. 2008; 36:D469–D474. [PubMed: 18032431]
6. Yamada M, Saier MH Jr. Glucitol-specific enzymes of the phosphotransferase system in *Escherichia coli*. Nucleotide sequence of the gut operon. J Biol Chem. 1987; 262:5455–5463. [PubMed: 3553176]
7. Zuluaga AF, Salazar BE, Rodriguez CA, Zapata AX, Agudelo M, Vesga O. Neutropenia induced in outbred mice by a simplified low-dose cyclophosphamide regimen: Characterization and applicability to diverse experimental models of infectious diseases. BMC Infect Dis. 2006; 6:55. [PubMed: 16545113]
8. Chalmers JD, Taylor JK, Singanayagam A, Fleming GB, Akram AR, Mandal P, Choudhury G, Hill AT. Epidemiology, antibiotic therapy, and clinical outcomes in health care-associated pneumonia: A UK cohort study. Clin Infect Dis. 2011; 53:107–113. [PubMed: 21690616]
9. Kollef MH, Shorr A, Tabak YP, Gupta V, Liu LZ, Johannes RS. Epidemiology and outcomes of health-care–associated pneumonia: Results from a large US database of culture-positive pneumonia. Chest. 2005; 128:3854–3862. [PubMed: 16354854]
10. Garbati MA, Al Godhair AI. The growing resistance of *Klebsiella pneumoniae*; the need to expand our antibiogram: Case report and review of the literature. Afr J Infect Dis. 2013; 7:8–10. [PubMed: 24381721]
11. McKenna M. Antibiotic resistance: The last resort. Nature. 2013; 499:394–396. [PubMed: 23887414]
12. Nordmann P, Dortet L, Poirel L. Carbapenem resistance in Enterobacteriaceae: Here is the storm! Trends Mol Med. 2012; 18:263–272. [PubMed: 22480775]
13. CDC. Vital signs: Carbapenem-resistant Enterobacteriaceae. MMWR Morb Mortal Wkly Rep. 2013; 62:165–170. [PubMed: 23466435]
14. Melzer M, Petersen I. Mortality following bacteraemic infection caused by extended spectrum beta-lactamase (ESBL) producing *E. coli compared to non-ESBL producing E. coli*. J Infect. 2007; 55:254–259. [PubMed: 17574678]
15. Bates DW, Sands K, Miller E, Lanken PN, Hibberd PL, Graman PS, Schwartz JS, Kahn K, Snydman DR, Parsonnet J, Moore R, Black E, Johnson BL, Jha A, Platt R. Predicting bacteremia in patients with sepsis syndrome. Academic Medical Center Consortium Sepsis Project Working Group. J Infect Dis. 1997; 176:1538–1551. [PubMed: 9395366]

NIH-PA Author Manuscript

NIH-PA Author Manuscript

NIH-PA Author Manuscript

16. Nakamura T, Takahashi O, Matsui K, Shimizu S, Setoyama M, Nakagawa M, Fukui T, Morimoto T. Clinical prediction rules for bacteremia and in-hospital death based on clinical data at the time of blood withdrawal for culture: An evaluation of their development and use. J Eval Clin Pract. 2006; 12:692–703. [PubMed: 17100868]
17. Owens, RC., Jr; Ambrose, PG.; Nightingale, CH., editors. Antibiotic Optimization: Concepts and Strategies in Clinical Practice. 1. Marcel Dekker; New York: 2005.
18. Scott, RD. The Direct Medical Costs of Healthcare-Associated Infections in US Hospitals and the Benefits of Prevention. Centers for Disease Control and Prevention; 2009.
19. Fischer BM, Olsen MW, Ley CD, Klausen TL, Mortensen J, Hojgaard L, Kristjansen PE. How few cancer cells can be detected by positron emission tomography? A frequent question addressed by an in vitro study. Eur J Nucl Med Mol Imaging. 2006; 33:697–702. [PubMed: 16612588]
20. König C, Simmen HP, Blaser J. Bacterial concentrations in pus and infected peritoneal fluid—Implications for bactericidal activity of antibiotics. J Antimicrob Chemother. 1998; 42:227–232. [PubMed: 9738841]
21. Jang K, Lee DH, Lee SH, Chung BH. Treatment of prostatic abscess: Case collection and comparison of treatment methods. Korean J Urol. 2012; 53:860–864. [PubMed: 23301131]
22. Yamamoto M, Fukushima T, Hirakawa K, Kimura H, Tomonaga M. Treatment of bacterial brain abscess by repeated aspiration—Follow up by serial computed tomography. Neurol Med Chir. 2000; 40:98–104. discussion 104–105.
23. Mease RC, Foss CA, Pomper MG. PET imaging in prostate cancer: Focus on prostate-specific membrane antigen. Curr Top Med Chem. 2013; 13:951–962. [PubMed: 23590171]
24. Scott ME, Viola RE. The use of fluoro- and deoxy-substrate analogs to examine binding specificity and catalysis in the enzymes of the sorbitol pathway. Carbohydr Res. 1998; 313:247–253. [PubMed: 10209867]
25. Ning X, Lee S, Wang Z, Kim D, Stubblefield B, Gilbert E, Murthy N. Maltodextrin-based imaging probes detect bacteria in vivo with high sensitivity and specificity. Nat Mater. 2011; 10:602–607. [PubMed: 21765397]
26. van Oosten M, Schäfer T, Gazendam JA, Ohlsen K, Tsompanidou E, de Goffau MC, Harmsen HJ, Crane LM, Lim E, Francis KP, Cheung L, Olive M, Ntziachristos V, van Dijl JM, van Dam GM. Real-time in vivo imaging of invasive- and biomaterial-associated bacterial infections using fluorescently labelled vancomycin. Nat Commun. 2013; 4:2584. [PubMed: 24129412]
27. Hernandez FJ, Huang L, Olson ME, Powers KM, Hernandez LI, Meyerholz DK, Thedens DR, Behlke MA, Horswill AR, McNamara JO II. Noninvasive imaging of *Staphylococcus aureus* infections with a nuclease-activated probe. Nat Med. 2014; 20:301–306. [PubMed: 24487433]
28. Kong Y, Yao H, Ren H, Subbian S, Cirillo SL, Sacchettini JC, Rao J, Cirillo JD. Imaging tuberculosis with endogenous β-lactamase reporter enzyme fluorescence in live mice. Proc Natl Acad Sci USA. 2010; 107:12239–12244. [PubMed: 20566877]
29. James ML, Gambhir SS. A molecular imaging primer: Modalities, imaging agents, and applications. Physiol Rev. 2012; 92:897–965. [PubMed: 22535898]
30. Vinjamuri S, Hall AV, Solanki KK, Bomanji J, Siraj Q, O'Shaughnessy E, Das SS, Britton KE. Comparison of 99mTc infecton imaging with radiolabelled white-cell imaging in the evaluation of bacterial infection. Lancet. 1996; 347:233–235. [PubMed: 8551884]
31. Nibbering PH, Welling MM, Paulusma-Annema A, Brouwer CP, Lupetti A, Pauwels EK. ^{99m}Tc-Labeled UBI 29-41 peptide for monitoring the efficacy of antibacterial agents in mice infected with *Staphylococcus aureus*. J Nucl Med. 2004; 45:321–326. [PubMed: 14960656]
32. Sarda L, Crémieux AC, Lebellec Y, Meulemans A, Lebtahi R, Hayem G, Génin R, Delahaye N, Huten D, Le Guludec D. Inability of ^{99m}Tc-ciprofloxacin scintigraphy to discriminate between septic and sterile osteoarticular diseases. J Nucl Med. 2003; 44:920–926. [PubMed: 12791820]
33. Sarda L, Saleh-Mghir A, Peker C, Meulemans A, Crémieux AC, Le Guludec D. Evaluation of ^{99m}Tc-ciprofloxacin scintigraphy in a rabbit model of *Staphylococcus aureus* prosthetic joint infection. J Nucl Med. 2002; 43:239–245. [PubMed: 11850491]
34. Dumarey N, Schoutens A. Renal abscess: Filling in with Tc-99m ciprofloxacin of defects seen on Tc-99m DMSA SPECT. Clin Nucl Med. 2003; 28:68–69. [PubMed: 12493973]

NIH-PA Author Manuscript

NIH-PA Author Manuscript

NIH-PA Author Manuscript

35. Langer O, Brunner M, Zeitlinger M, Ziegler S, Muller U, Dobrozemsky G, Lackner E, Joukhadar C, Mitterhauser M, Wadsak W, Minar E, Dudczak R, Kletter K, Muller M. In vitro and in vivo evaluation of [^{18}F]ciprofloxacin for the imaging of bacterial infections with PET. Eur J Nucl Med Mol Imaging. 2005; 32:143–150. [PubMed: 15690222]
36. Welling M, Stokkel M, Balter J, Sarda-Mantel L, Meulemans A, Le Guludec D. The many roads to infection imaging. Eur J Nucl Med Mol Imaging. 2008; 35:848–849. [PubMed: 18188558]
37. Panizzi P, Nahrendorf M, Figueiredo JL, Panizzi J, Marinelli B, Iwamoto Y, Keliher E, Maddur AA, Waterman P, Kroh HK, Leuschner F, Aikawa E, Swirski FK, Pittet MJ, Hackeng TM, Fuentes-Prior P, Schneewind O, Bock PE, Weissleder R. In vivo detection of *Staphylococcus aureus* endocarditis by targeting pathogen-specific prothrombin activation. Nat Med. 2011; 17:1142–1146. [PubMed: 21857652]
38. Bettegowda C, Foss CA, Cheong I, Wang Y, Diaz L, Agrawal N, Fox J, Dick J, Dang LH, Zhou S, Kinzler KW, Vogelstein B, Pomper MG. Imaging bacterial infections with radio-labeled 1-(2¢-deoxy-2¢-fluoro-β-D-arabinofuranosyl)-5-iodouracil. Proc Natl Acad Sci USA. 2005; 102:1145–1150. [PubMed: 15653773]
39. Wyss MT, Honer M, Späth N, Gottschalk J, Ametamey SM, Weber B, von Schulthess GK, Buck A, Kaim AH. Influence of ceftriaxone treatment on FDG uptake—An in vivo [^{18}F]-fluorodeoxyglucose imaging study in soft tissue infections in rats. Nucl Med Biol. 2004; 31:875–882. [PubMed: 15464389]
40. Davis SL, Nuermberger EL, Um PK, Vidal C, Jedynak B, Pomper MG, Bishai WR, Jain SK. Noninvasive pulmonary [^{18}F]-2-fluoro-deoxy-D-glucose positron emission tomography correlates with bactericidal activity of tuberculosis drug treatment. Antimicrob Agents Chemother. 2009; 53:4879–4884. [PubMed: 19738022]
41. Jain SK, Kwon P, Moss WJ. Management and outcomes of intracranial tuberculomas developing during antituberculous therapy: Case report and review. Clin Pediatr. 2005; 44:443–450.
42. Sievers F, Wilm A, Dineen D, Gibson TJ, Karplus K, Li W, Lopez R, McWilliam H, Remmert M, Söding J, Thompson JD, Higgins DG. Fast, scalable generation of high-quality protein multiple sequence alignments using Clustal Omega. Mol Syst Biol. 2011; 7:539. [PubMed: 21988835]
43. Rouse, M.; Steckelberg, JM. Handbook of Animal Models of Infection. Zak, O.; Sande, MA., editors. Vol. chap 58. Academic Press; London: 1999. p. 495-500.
44. Gonzalez-Perez O, Guerrero-Cazares H, Quiñones-Hinojosa A. Targeting of deep brain structures with microinjections for delivery of drugs, viral vectors, or cell transplants. J Vis Exp. 2010:2082. [PubMed: 21178958]
45. van Ogtrop ML, Mattie H, Guiot HF, van Strijen E, Hazekampvan Dokkum AM, van Furth R. Comparative study of the effects of four cephalosporins against *Escherichia coli* in vitro and in vivo. Antimicrob Agents Chemother. 1990; 34:1932–1937. [PubMed: 2291658]

NIH-PA Author Manuscript NIH-PA Author Manuscript NIH-PA Author Manuscript

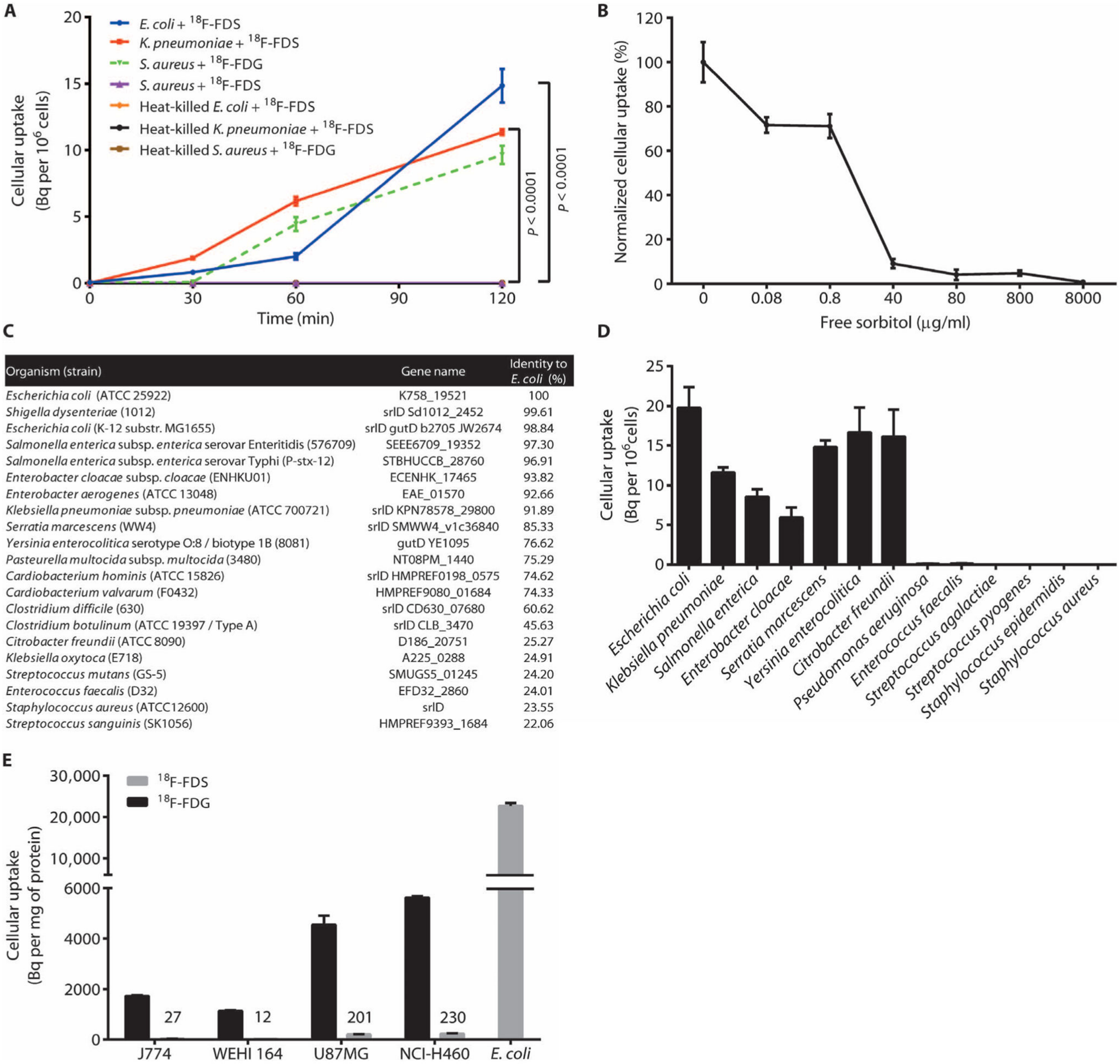

Organism (strain)	Gene name	Identity to *E. coli* (%)
Escherichia coli (ATCC 25922)	K758_19521	100
Shigella dysenteriae (1012)	srlD Sd1012_2452	99.61
Escherichia coli (K-12 substr. MG1655)	srlD gutD b2705 JW2674	98.84
Salmonella enterica subsp. *enterica* serovar Enteritidis (576709)	SEEE6709_19352	97.30
Salmonella enterica subsp. *enterica* serovar Typhi (P-stx-12)	STBHUCCB_28760	96.91
Enterobacter cloacae subsp. *cloacae* (ENHKU01)	ECENHK_17465	93.82
Enterobacter aerogenes (ATCC 13048)	EAE_01570	92.66
Klebsiella pneumoniae subsp. *pneumoniae* (ATCC 700721)	srlD KPN78578_29800	91.89
Serratia marcescens (WW4)	srlD SMWW4_v1c36840	85.33
Yersinia enterocolitica serotype O:8 / biotype 1B (8081)	gutD YE1095	76.62
Pasteurella multocida subsp. *multocida* (3480)	NT08PM_1440	75.29
Cardiobacterium hominis (ATCC 15826)	srlD HMPREF0198_0575	74.62
Cardiobacterium valvarum (F0432)	HMPREF9080_01684	74.33
Clostridium difficile (630)	srlD CD630_07680	60.62
Clostridium botulinum (ATCC 19397 / Type A)	srlD CLB_3470	45.63
Citrobacter freundii (ATCC 8090)	D186_20751	25.27
Klebsiella oxytoca (E718)	A225_0288	24.91
Streptococcus mutans (GS-5)	SMUGS5_01245	24.20
Enterococcus faecalis (D32)	EFD32_2860	24.01
Staphylococcus aureus (ATCC12600)	srlD	23.55
Streptococcus sanguinis (SK1056)	HMPREF9393_1684	22.06

Fig. 1. In vitro uptake of ^{18}F-FDS in bacterial pathogens and mammalian cell lines

(**A**) ^{18}F-FDS uptake in *E. coli* (ATCC 25922), *K. pneumoniae* (ATCC 35657), and *S. aureus* (ATCC 29213) cultures incubated with ^{18}F-FDS or ^{18}F-FDG. Heat-killed bacteria were negative controls. *P* values compared to respective heat-killed controls were determined by two-tailed Student's *t* test. (**B**) Competition of ^{18}F-FDS uptake with increasing concentrations of unlabeled (free) sorbitol in *E. coli* (normalized to *E. coli* uptake without sorbitol). (**C**) Homology of *E. coli* (ATCC 25922) sorbitol-6-phosphate dehydrogenase gene, *srlD*, to other pathogenic bacteria in the UniProtKB database. (**D**) Uptake of ^{18}F-FDS in ATCC reference Gram-negative and Gram-positive bacterial strains incubated for 120 min. (**E**) J774 (murine macrophage), WEHI 164 (murine fibroblast), U87MG (human

NIH-PA Author Manuscript

NIH-PA Author Manuscript

NIH-PA Author Manuscript

glioblastoma), and NCI-H460 (human large cell lung carcinoma) cultures were incubated with ^{18}F-FDS or ^{18}F-FDG. Uptake was measured at 120 min and is shown in comparison to the reference *E. coli*. Data in (A), (B), (D), and (E) are means ± SEM ($n = 6$).

NIH-PA Author Manuscript
NIH-PA Author Manuscript
NIH-PA Author Manuscript

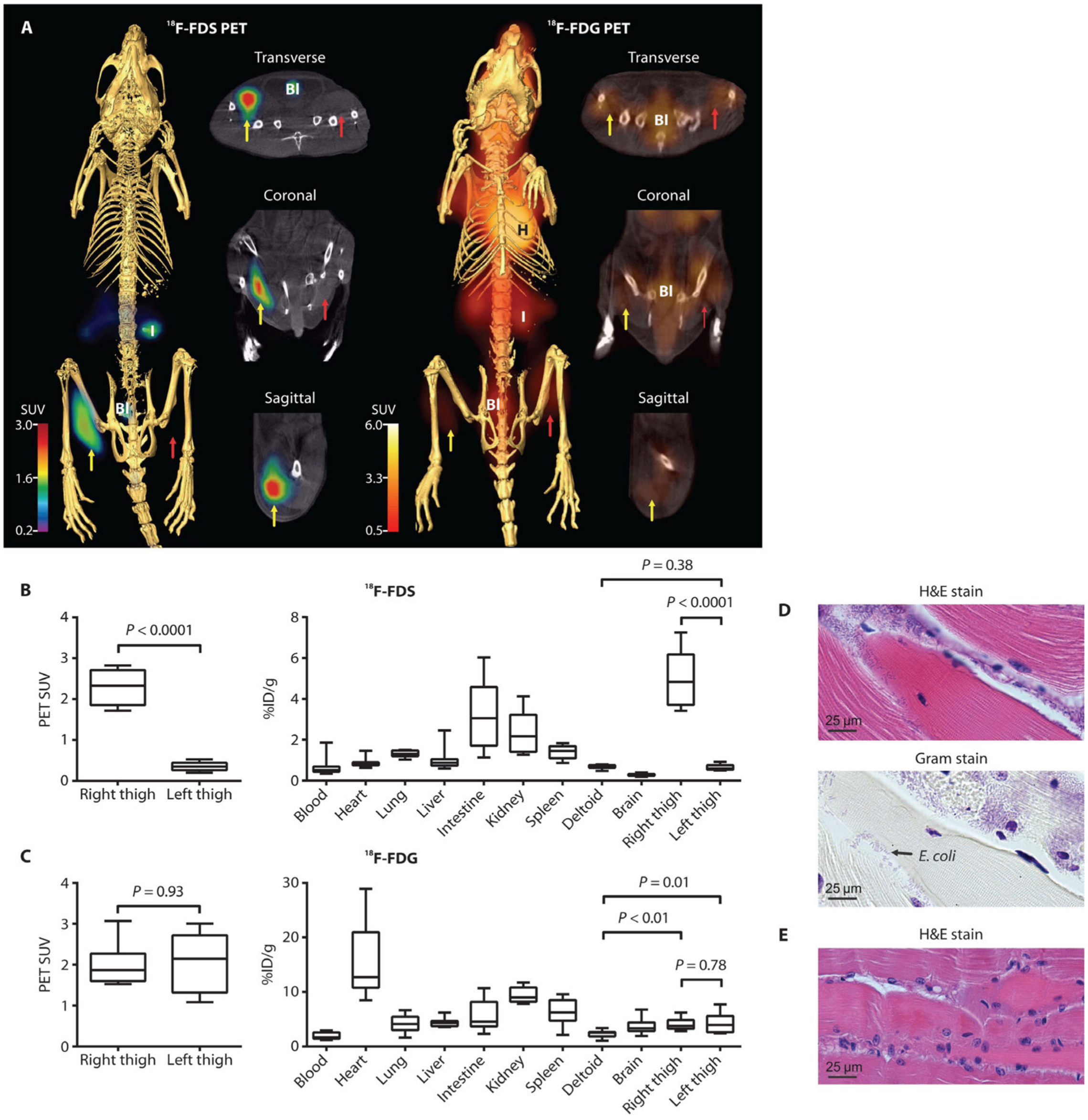

Fig. 2. PET/CT imaging of *E. coli* myositis in immunocompetent mice

(**A**) ^{18}F-FDS signal is noted in the infected (yellow arrow) but not in the inflamed (control) sterile thigh (red arrow). ^{18}F-FDG signal was noted in both infected and inflamed thighs. H, heart; I, intestine; Bl, bladder. (**B** and **C**) ^{18}F-FDS (B) and ^{18}F-FDG (C) PET signals in vivo from the infected (right) and inflamed (left) thighs and postmortem biodistribution in all organs. Data are medians with interquartile and ranges shown ($n = 8$ animals for ^{18}F-FDS and $n = 9$ for ^{18}F-FDG). P values were determined by two-tailed Mann-Whitney U test. (**D** and **E**) Hematoxylin and eosin (H&E) and Gram stains with inflammatory cells and Gram-negative bacteria in the *E. coli*–infected (right) thigh (D) and inflammatory cells without bacteria in the inflamed (left) thigh (E). Images are representative of five animals.

NIH-PA Author Manuscript
NIH-PA Author Manuscript
NIH-PA Author Manuscript

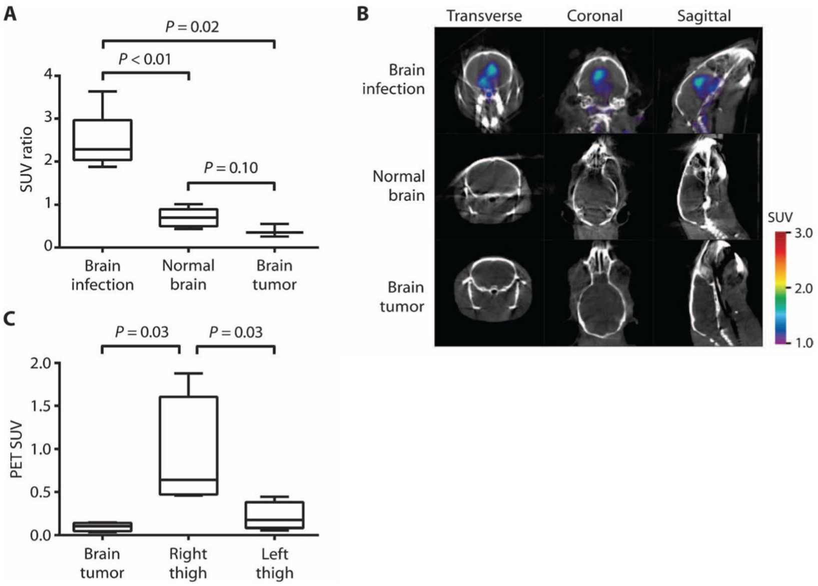

Fig. 3. ^{18}F-FDS PET/CT imaging of human brain tumor xenograft versus *E. coli* infection

(**A**) ^{18}F-FDS PET signal from an *E. coli*–infected brain compared with a human brain tumor (U87MG) xenograft and normal brain. Data are median SUV ratios normalized to the uninflamed thigh muscle of each animal, with interquartile and ranges shown ($n = 6$ animals for brain infection, $n = 6$ for normal brain, and $n = 3$ for brain tumor). (**B**) ^{18}F-FDS PET signal in the *E. coli*–infected brain, normal brain, or tumor brain tissues. (**C**) ^{18}F-FDS PET signal from right-thigh *E. coli* infection compared with human brain tumor (U87MG) xenograft and infected left thigh in the same animals. Data are median SUVs with interquartile and ranges shown ($n = 4$ animals). *P* values in (A) and (C) were determined by two-tailed Mann-Whitney *U* test.

NIH-PA Author Manuscript

NIH-PA Author Manuscript

NIH-PA Author Manuscript

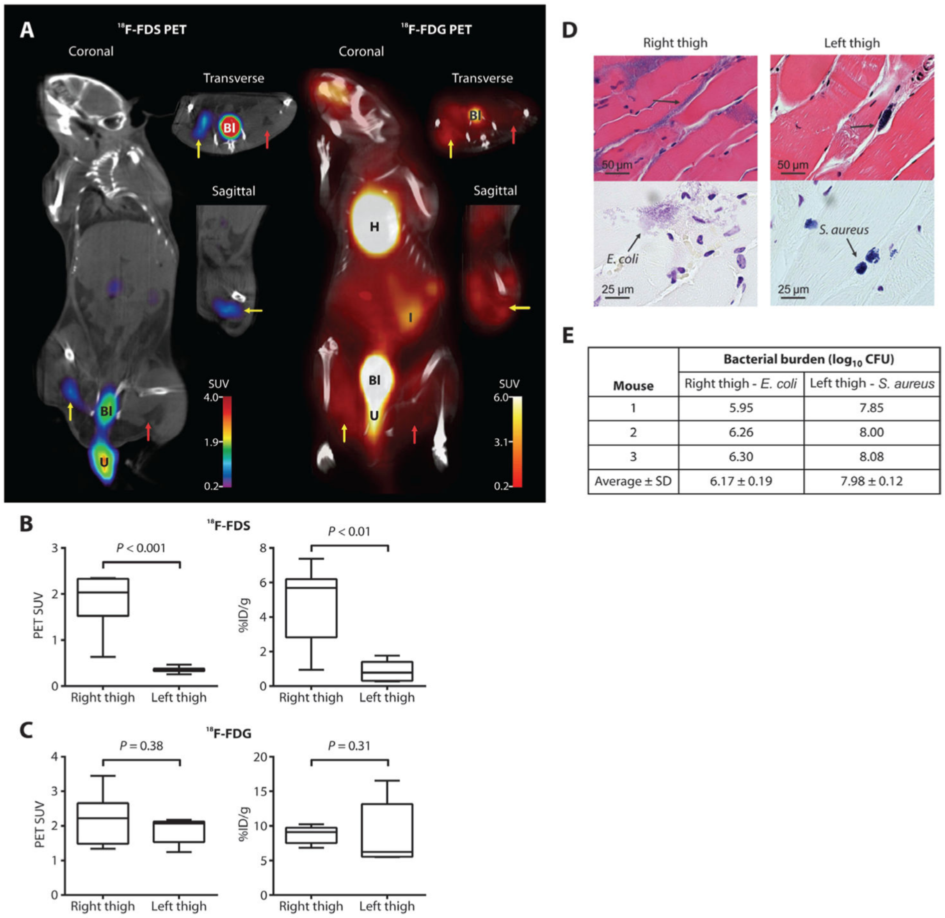

Mouse	Bacterial burden ($\log_{10}$ CFU)	
	Right thigh - *E. coli*	Left thigh - *S. aureus*
1	5.95	7.85
2	6.26	8.00
3	6.30	8.08
Average ± SD	6.17 ± 0.19	7.98 ± 0.12

Fig. 4. PET/CT imaging of mixed myositis thigh infection

(**A**) ^{18}F-FDS PET signal was observed in the *E. coli*–infected right thigh (yellow arrow), but not in the *S. aureus*–infected left thigh (red arrow). ^{18}F-FDG signal was noted in both *E. coli*– and *S. aureus*–infected thighs. U, extravasated urine. (**B** and **C**) ^{18}F-FDS (B) and ^{18}F-FDG (C) PET signals in vivo from the infected thighs and postmortem biodistribution. Data are medians with in-terquartile and ranges shown ($n = 7$ animals each for ^{18}F-FDS and ^{18}F-FDG). P values were determined by two-tailed Mann-Whitney U test. (**D**) H&E and Gram stains demonstrating Gram-negative (right thigh) and Gram-positive (left thigh) bacteria. Images are representative of five animals. (**E**) Bacterial burden immediately after completion of ^{18}F-FDS PET imaging in each mouse ($n = 3$) in one of the dually infected imaging cohorts.

NIH-PA Author Manuscript

NIH-PA Author Manuscript

NIH-PA Author Manuscript

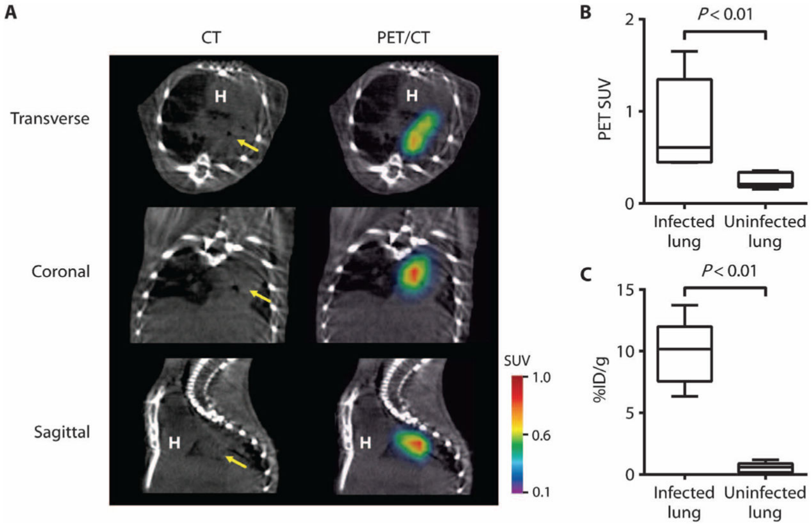

Fig. 5. ***K. pneumoniae* lung infection (pneumonia)**

(**A**) ^{18}F-FDS PET signal colocalized with *K. pneumoniae* lung infection noted on CT (yellow arrow). (**B** and **C**) ^{18}F-FDS PET signal in vivo (B) and postmortem bio-distribution (C) in infected versus uninfected lungs. Data are medians with interquartile and ranges shown (*n* = 5 animals for the infected group and *n* = 6 for the uninfected group).

NIH-PA Author Manuscript
NIH-PA Author Manuscript
NIH-PA Author Manuscript

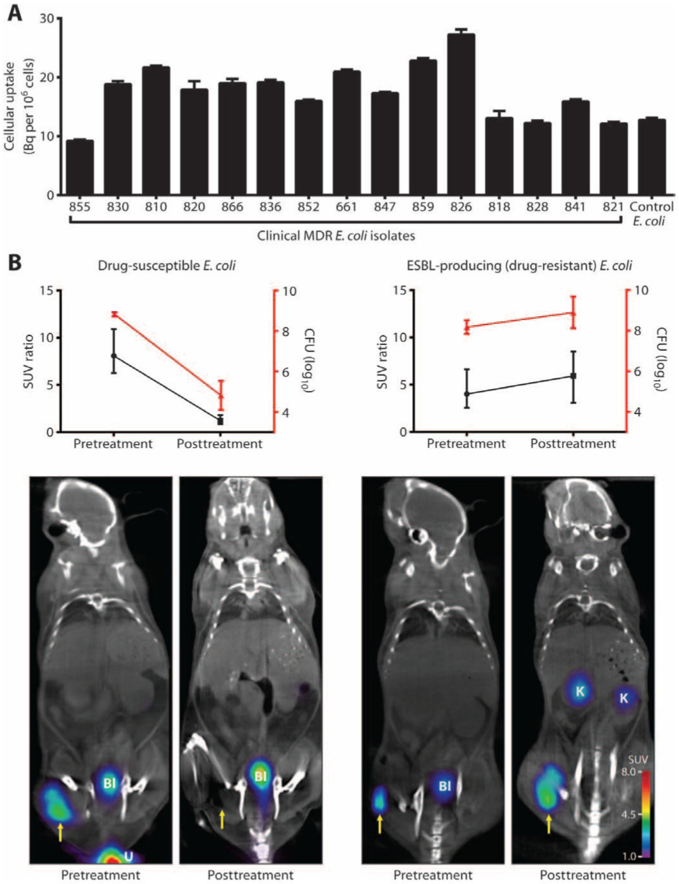

Fig. 6. ^{18}F-FDS PET/CT monitoring of antimicrobial efficacy

(**A**) In vitro ^{18}F-FDS uptake in 15 MDR *E. coli* (ESBL-producing) clinical strains. Uptake was measured at 120 min and is shown in comparison to the reference *E. coli* (positive control). Data are means ± SEM (*n* = 6). (**B**) Animals were inoculated with drug-susceptible (*n* = 5) or drug-resistant (ESBL-producing; *n* = 6) *E. coli* and treated with ceftriaxone for 24 hours. Antimicrobial treatment efficacy was measured as CFU and PET signal intensity. Yellow arrow indicates infected right thigh. K, kidney. Data are means ± SD (CFU) and medians and ranges (SUV ratio).